JGR Atmospheres

RESEARCH ARTICLE
10.1029/2025JD045948

The Wet Bias of Winter Precipitation Over Western Tibetan Plateau in RegCM4 Reduced by Including Anisotropic Topographic Factors in Sub-Grid Turbulent Orographic Form Drag Scheme

Chunlei Gu[1], Anning Huang[1,2], Xin Li[3], Xiaoke Xu[4], and Yang Wu[3]

[1]School of Atmospheric Sciences, Nanjing University, Nanjing, China, [2]Qinghai Lake Comprehensive Observation Research Station, Chinese Academy of Sciences, Gangcha, China, [3]Nanjing Innovation Institute for Atmospheric Sciences, Chinese Academy of Meteorological Sciences-Jiangsu Meteorological Service, Jiangsu Key Laboratory of Severe Storm Disaster Risk/Key Laboratory of Transportation Meteorology of CMA, Nanjing, China, [4]School of Geographical Sciences, Southwest University, Chongqing, China

Abstract The circulation and precipitation over complex terrains can be clearly influenced by the sub-grid turbulent orographic form drag (STOFD). This study refines the Beljaars STOFD scheme by incorporating the anisotropic topographic factors. Both the original and modified STOFD schemes were implemented in the Regional Climate Model Version 4 (RegCM4). Results show that both STOFD schemes effectively reduce the overestimation of winter precipitation by the RegCM4 over the western Tibetan Plateau (TP). Adopting the original STOFD scheme increases the correlation coefficient (CC) and Taylor score (TS) of simulated winter precipitation over the western TP by 2.6% and 17.5%, respectively, while reducing the root mean square error (RMSE) by 16.3%. Compared to the original scheme, using the modified STOFD scheme further improves the TS (CC) by 6.4% (1.3%) and decreases the RMSE by 6.3%, indicating that winter precipitation simulation in the western TP is further enhanced. Mechanism analysis indicates that the suppression of overestimated precipitation results from the weakened simulation of vertical motion and water vapor transport, which are caused by the attenuated westerly winds due to the STOFD scheme. The significant reduced precipitation on the windward slope is attributed to the combined effects of anomalous downward motion and negative water vapor transport anomalies. Conversely, changes in precipitation simulation on the leeward slope are not significant, which results from the mutually offsetting influences of anomalous upward motion and negative water vapor transport anomalies. This study indicates the importance of considering the anisotropic topographic effects in the STOFD scheme.

Plain Language Summary This study updates the Beljaars STOFD scheme by incorporating the anisotropic topographic factors. The original and updated schemes are implemented in the Regional Climate Model Version 4 (RegCM4). Results show that the overestimated winter precipitation over the western Tibetan Plateau (TP) by the RegCM4 can be clearly reduced by adopting each of the STOFD schemes, and the updated one performs better than the original one. Relative to the original STOFD scheme, adopting the updated one can lead to an additional increase of 6.4% (1.3%) in the Taylor score (correlation coefficient) of winter precipitation simulation over the western TP, along with an additional reduction of 6.3% in the root mean square error. The reduced precipitation simulation results from the weakened simulation of water vapor transport and upward motion, which in turn stems from the decreased simulation of the west wind induced by the STOFD. The significant reduction in precipitation simulation on the windward slope is attributed to the combined effects of weakened upward motion and reduced water vapor transport. Conversely, on the leeward slope, the effects of weakened ascending motion and reduced water vapor transport largely offset each other, resulting in only minor changes in simulated precipitation.

Key Points:

- The STOFD scheme is modified by incorporating anisotropic terrain factors derived from high-resolution elevation data
- The more realistic of sub-grid topographic depiction in the modified STOFD scheme leads to improved westerly moisture transport simulation
- The modified STOFD scheme further reduces the winter precipitation overestimation over the western Tibetan Plateau in RegCM4

Correspondence to:
A. Huang,
anhuang@nju.edu.cn

Citation:
Gu, C., Huang, A., Li, X., Xu, X., & Wu, Y. (2026). The wet bias of winter precipitation over western Tibetan Plateau in RegCM4 reduced by including anisotropic topographic factors in sub-grid turbulent orographic form drag scheme. *Journal of Geophysical Research: Atmospheres*, *131*, e2025JD045948. https://doi.org/10.1029/2025JD045948

Received 21 NOV 2025
Accepted 20 MAY 2026

Author Contributions:
Conceptualization: Anning Huang
Data curation: Chunlei Gu, Anning Huang, Xin Li, Xiaoke Xu, Yang Wu
Formal analysis: Chunlei Gu, Anning Huang, Xin Li
Investigation: Chunlei Gu, Yang Wu
Methodology: Chunlei Gu, Anning Huang
Resources: Chunlei Gu, Anning Huang, Xin Li, Xiaoke Xu, Yang Wu
Software: Chunlei Gu
Supervision: Anning Huang
Validation: Chunlei Gu
Visualization: Chunlei Gu
Writing – original draft: Chunlei Gu, Anning Huang
Writing – review & editing: Chunlei Gu, Anning Huang, Xin Li, Xiaoke Xu, Yang Wu

1. Introduction

The Tibetan Plateau (TP) exerts substantial thermal and dynamic influences on the Asian monsoon system, with far-reaching implications for global atmospheric circulation patterns (Huang et al., 2023; Wu et al., 2022). The TP is known as the "Asian Water Tower." Its western region is the origin of important rivers such as the Indus, Amu Darya, and Tarim Rivers, where precipitation mainly consists of winter rainfall driven by moisture transported by

the westerlies (Curio & Scherer, 2016; Liu et al., 2020; Ma et al., 2018; Rahimi et al., 2019). Precipitation in the western TP significantly influences the distribution of regional water resources, the maintenance of ecological balance, and the water supply of major downstream Asian rivers (Li et al., 2020; Mao et al., 2024; Wang et al., 2017). Therefore, improving the precipitation simulation and prediction in this area is critically important.

The TP features complex terrain and intense land-atmosphere interactions, such as orographic forcing, uplift, and active turbulent exchange, making it a challenging region for the performance of many numerical models (Guo et al., 2018; Karim et al., 2025; Li et al., 2022; Wang et al., 2020). Currently, the various numerical models tend to underestimate temperatures during cold seasons and overestimate precipitation throughout the year in the TP (Cui et al., 2021; Fu et al., 2021; Hu et al., 2022; Li et al., 2023). Systematic errors in numerical models over the TP pose significant challenges to regional climate prediction and ecological conservation (Bao & Li, 2020; Ma et al., 2023). These biases partly arise from limitations in the parameterizations of sub-grid scale processes, such as convection, thermal effects, terrain-induced drag, and orographic precipitation triggering mechanisms (Gu et al., 2020; Li, Lu, et al., 2024; Su et al., 2013).

By enhancing the representation of cloud cover, incoming longwave radiation flux, surface snow cover, and land-atmosphere interaction processes in the numerical models, the cold bias of the simulated temperature over the TP can be partially mitigated (Gu et al., 2024; Li, Gao, et al., 2024; Luo et al., 2025; Yue et al., 2021). Improving model resolution, representing land-atmosphere interactions more realistically, employing a convection-permitting model, and refining cloud processes can reduce the wet bias in the simulation of summer precipitation over the TP (Gu et al., 2022; Lin et al., 2018; Liu et al., 2022, 2024; Wang et al., 2021; Yang & Wang, 2022; Zhao et al., 2023). In addition, various numerical models also overestimate winter precipitation in the TP (Li et al., 2023; Rahimi et al., 2019; Zou & Zhou, 2024). A recent study shows that adopting the sub-grid turbulent orographic form drag (STOFD) parameterization can improve the simulated precipitation in the western TP during December 2007 with the Weather Research and Forecasting Model (Zhou et al., 2019).

The STOFD refers to the turbulence induced by small-scale topography, leading to the turbulent breakdown and slowed atmospheric flow (Koo et al., 2018; Zhou et al., 2017). The effective roughness length method and the distributed method have been used to parameterize STOFD (Emeis & Zilitinkevich, 1991; Wood et al., 2001). Typically, the roughness length in models is determined by underlying surface types and vegetation, while the effective roughness length also accounts for sub-grid terrain features and improves the simulation of drag forces in rugged regions (Fiedler & Panofsky, 1972; Weissel et al., 1994). The effective roughness length method is relatively simple and widely used but has non-negligible shortcomings and errors (Liu et al., 2019; Lorente-Plazas et al., 2016; Zhou et al., 2017). Therefore, the distributed STOFD scheme is designed to directly apply terrain-induced turbulent drag forces to the horizontal wind components across multiple model layers (Wilson, 2002; Wood et al., 2001). The distributed STOFD scheme proposed by Beljaars et al. (2004) is applicable to numerical models with various horizontal resolutions and different configurations (Gu et al., 2023; Sandu et al., 2016; Xue et al., 2021; Zhou et al., 2018). However, in the Beljaars STOFD scheme, the small-scale terrain-related factors are derived by filtering elevation data at a horizontal resolution of 30″ (∼1 km), which cannot fully capture fine-scale topographic features. Additionally, the Beljaars scheme treats the STOFD as isotropic. Given that elevation data at very high horizontal resolution now cover the entire globe (Farr et al., 2008; Fujisada et al., 2012; Grohmann, 2018), it has become feasible to directly utilize these high-resolution elevation data sets to generate the STOFD scheme. Therefore, Xue and Shen (2023) developed an anisotropic STOFD parameterization scheme using the elevation data at a horizontal resolution of 3″ (∼90 m), specifically designed for numerical models with horizontal resolutions ranging from kilometers to sub-kilometers.

The Regional Climate Model Version 4 (RegCM4), widely applied to East Asia, also significantly overestimates the winter precipitation over the TP (Gao et al., 2017; Gao & Giorgi, 2017; Gu et al., 2020). The Beljaars STOFD scheme has been demonstrated to enhance the RegCM4's simulation of summer monsoon precipitation in eastern China (Gu et al., 2023). Specifically, the STOFD scheme enhances precipitation simulation in southeastern China by generating more concentrated disturbances, while its remote effects significantly influence atmospheric circulation and improve precipitation simulation in northern China (Zhou et al., 2024). However, the influence of the STOFD scheme on RegCM4's performance in simulating the winter precipitation over the TP remains unexplored.

Based on this background, three key research questions emerge: (a) Can the integration of high-resolution elevation data into the Beljaars STOFD scheme improve its representation of sub-grid scale terrain processes?

(b) To what extent do the modified and original STOFD schemes differ in their impacts on RegCM4's performance during winter over the western TP? And (c) What are the underlying physical mechanisms? To address these questions, this study enhances the Beljaars STOFD scheme by transitioning it from an isotropic to an anisotropic formulation using high-resolution elevation data at a horizontal resolution of 1″ (~30 m). The research systematically evaluates and compares the effects of both the original and modified STOFD schemes on the performance of RegCM4 in simulating the winter precipitation over the TP.

The remainder of this paper is structured as follows. Section 2 describes the Beljaars STOFD scheme and presents its modification. Section 3 introduces the data, model configuration, and experimental design. Section 4 evaluates and compares the performance of RegCM4 adopting the original and modified STOFD schemes in simulating winter climate over the western TP. Section 5 indicates the physical mechanisms underlying the differences induced by the two schemes. Finally, Section 6 summarizes the key findings and provides discussions.

2. Introduction of the STOFD Schemes

2.1. Original Beljaars STOFD Scheme

Beljaars et al. (2004) developed an STOFD scheme that directly applies to the horizontal wind components at each vertical model level. Within this scheme, the STOFD can be calculated according to Equation 1.

$$\frac{\partial}{\partial z}\left(\frac{\tau_o}{\rho}\right) = -2.109\alpha\beta C_{\mathrm{md}} C_{\mathrm{corr}} \vec{V}\left|\vec{V}\right| e^{-\left(\frac{z}{1500}\right)^{1.5}} z^{-1.2} a_2 \tag{1}$$

Where $\alpha = 12$, $\beta = 1$, $C_{\mathrm{md}} = 0.005$, and $C_{\mathrm{corr}} = 0.6$. $\vec{V}$ represents the horizontal wind vector at various vertical levels, with u and v as its two components. The wind speed is denoted by $\left|\vec{V}\right| = \sqrt{u^2 + v^2}$. $e = 2.7182818$ is the base of the natural logarithm. z represents the height above ground at different vertical levels. In Equation 1, the only term associated with sub-grid small-scale topography is a_2. Here, a_2 represents the proportionality coefficient of the small-scale topographic spectral function $F(k)$ within the wavenumber range from $k = 0.003\ \mathrm{m}^{-1}$ to $k = 0.012\ \mathrm{m}^{-1}$. Substituting the constants mentioned above into Equation 1 results in Equation 2.

$$\frac{\partial}{\partial z}\left(\frac{\tau_o}{\rho}\right) = -7.5924 \times 10^{-2} a_2 \vec{V}\left|\vec{V}\right| e^{-\left(\frac{z}{1500}\right)^{1.5}} z^{-1.2} \tag{2}$$

The small-scale topographic spectral function can be expressed as a piecewise power-law function: $F(k) = \begin{cases} a_1 k^{n_1} & \text{for } 0.000628 < k \le 0.003 \\ a_2 k^{n_2} & \text{for } 0.003 < k \le 0.012 \end{cases}$. In this function, the power-law exponents $n_1 = -1.9$ and $n_2 = -2.8$ can be approximated as constants across various regions and intensities of small-scale topographic spectra. Therefore, the intensity of $F(k)$ is determined by the proportionality coefficients a_1 and a_2, which can be derived through Fast Fourier Transform (FFT) analysis using topographic elevation data with a horizontal resolution of tens of meters. However, due to the unavailability of globally accessible elevation data with this resolution at that time, the small-scale topographic spectral function was estimated using elevation data with a horizontal resolution of 30″ (~1 km) following Equations 3–5.

$$F_O(k) = \begin{cases} a_1 k^{n_1}, 0.000628 < k \le 0.003 \\ a_2 k^{n_2}, 0.003 < k \le 0.012 \end{cases} \tag{3}$$

$$a_1 = \sigma_{\mathrm{flt}}^2 \left(I_H k_{\mathrm{flt}}^{n_1}\right)^{-1} \tag{4}$$

$$a_2 = a_1 k_1^{(n_1 - n_2)} \tag{5}$$

where $n_1 = -1.9$, $n_2 = -2.8$, $k_1 = 0.003\ \mathrm{m}^{-1}$, $k_{\mathrm{flt}} = 0.00035\ \mathrm{m}^{-1}$, and $I_H = 0.00102\ \mathrm{m}^{-1}$. σ_{flt}^2 represents the sub-grid small-scale topographic filtering variance derived from the elevation data with a horizontal resolution of 30″ through filtering (details shown in the appendix of Beljaars et al., 2004). Substitute $a_2 = 1.4273755 \times 10^{-6} \sigma_{\mathrm{flt}}^2$ into Equation 2 to calculate the STOFD using Equation 6.

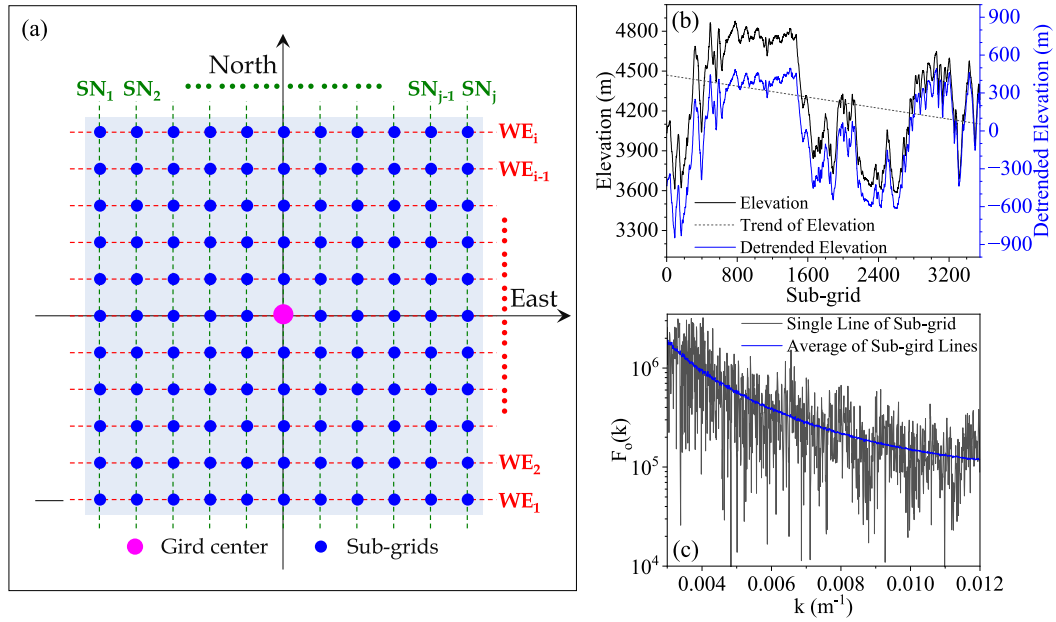

Figure 1. (a) Schematic diagram of sub-grid terrain sampling. (b) Example of a sub-grid terrain elevation sequence (black line), including its linear trend (dashed line) and the detrended elevation sequence (blue line). (c) Example of a single small-scale topographic spectrum alongside the grid-scale averaged small-scale topographic spectrum in the u direction.

$$\frac{\partial}{\partial z}\left(\frac{\tau_o}{\rho}\right) = -1.08372058 \times 10^{-7}\sigma_{\text{flt}}^2 \vec{V}\left|\vec{V}\right| e^{-\left(\frac{z}{1500}\right)^{1.5}} z^{-1.2} \tag{6}$$

The original Beljaars STOFD scheme described above has three limitations as follows: (a) It assumes identical power-law exponents ($n_1 = -1.9$ and $n_2 = -2.8$) for the small-scale topographic spectral function across all regions. This assumption cannot be disregarded; otherwise, the STOFD would need to be explicitly calculated at each grid, necessitating the construction of separate differential equations for each location. Such an approach would consume substantial computational resources and require the differential equations to be rebuilt whenever the model grid changes. (b) It assumes an isotropic STOFD, treating the small-scale topographic spectral functions in the u and v component directions as identical in the large grid cells. (c) It utilizes coarse-resolution elevation data rather than high-resolution data to extract the parameters for the small-scale topographic spectral function.

2.2. Modified STOFD Scheme

Currently, global coverage of topographic elevation data with horizontal resolutions of 1″ (~30 m) is available. Consequently, high-resolution elevation data can be utilized to directly resolve the small-scale topographic spectral functions for both u and v components, thereby eliminating errors associated with shortcomings (b) and (c). According to previous studies (Bannon & Yuhas, 1990; Beljaars et al., 2004; Young & Pielke, 1983), the method for resolving $F_o(k) = \text{ak}^n$ at model grids is as follows:

1. Sampling. As illustrated in Figure 1a, sampling is performed within the designated grid range. Horizontal intervals of 1″ (~30 m) are utilized to sample from west to east and from south to north, respectively, obtaining sub-grid terrain elevation sequences such as WE_1, WE_2, ……, WE_{i-1}, and WE_i in the west-east direction and SN_1, SN_2, ……, SN_{j-1}, and SN_j in the south-north direction. For example, the thin black line in Figure 1b represents WE_1.
2. The linear trend of the elevation sequences is eliminated using the least squares method. For example, the black dashed line in Figure 1b represents the linear trend of WE_1, while the blue polyline illustrates WE_1 after the linear trend has been removed. Removing the linear trend before performing a FFT primarily aims to

eliminate low-frequency interference caused by terrain with an infinite scale, thereby enhancing the accuracy and clarity of the spectral analysis.

3. The FFT is applied to the detrended elevation sequences to obtain the analyzed values of the small-scale topographic spectrum $F_{o,\mathrm{WE}_1}(k)$ corresponding to the WE_1 elevation sequence (e.g., the black polyline in Figure 1c).
4. Steps (2) and (3) are repeated to obtain the analytical values of the small-scale topographic spectra corresponding to the elevation sequences WE_1, WE_2, ……, WE_{i-1}, WE_i, SN_1, SN_2, ……, SN_{j-1}, and SN_j. These spectra are denoted as $F_{o,\mathrm{WE}_1}(k)$, $F_{o,\mathrm{WE}_2}(k)$, ……, $F_{o,\mathrm{WE}_{i-1}}(k)$, $F_{o,\mathrm{WE}_i}(k)$, $F_{o,\mathrm{SN}_1}(k)$, $F_{o,\mathrm{SN}_2}(k)$, ……, $F_{o,\mathrm{SN}_{j-1}}(k)$, and $F_{o,\mathrm{SN}_j}(k)$, respectively.
5. Calculate the grid-scale averaged small-scale topographic spectra in the u and v directions: $F_{o,\mathrm{WE}}(k) = \frac{1}{i}\sum_{m=1}^{m=i} F_{o,\mathrm{WE}_m}(k)$ and $F_{o,\mathrm{SN}}(k) = \frac{1}{j}\sum_{m=1}^{m=j} F_{o,\mathrm{WE}_m}(k)$. For Example, the blue line in Figure 1c represents the grid-scale averaged small-scale topographic spectrum in the u direction.
6. Based on $F_{o,\mathrm{WE}}(k)$, $F_{o,\mathrm{SN}}(k)$, and $F_O(k) = a_2 k^{-2.8}$ within the wavenumber range $0.003 < k \leq 0.012$, the grid-scale $a_{2,\mathrm{WE}}$ and $a_{2,\mathrm{SN}}$ for the u and v directions are calculated inversely, respectively.

According to Equations 2 and 6, the formulation for the STOFD can be expressed as Equations 7–9:

$$\frac{\partial}{\partial z}\left(\frac{\tau_o}{\rho}\right) = C_{\mathrm{TOFD}}\vec{V}\left|\vec{V}\right| e^{-\left(\frac{z}{1500}\right)^{1.5}} z^{-1.2} \tag{7}$$

$$C_{\mathrm{TOFD}} = C_{\mathrm{TOFD},o} = -1.08372058 \times 10^{-7}\sigma_{\mathrm{flt}}^2 \tag{8}$$

$$C_{\mathrm{TOFD}} = \begin{cases} C_{\mathrm{TOFD},u} = -7.5924 \times 10^{-2} a_{2,\mathrm{WE}} & \text{for } u \text{ direction} \\ C_{\mathrm{TOFD},v} = -7.5924 \times 10^{-2} a_{2,\mathrm{SN}} & \text{for } v \text{ direction} \end{cases} \tag{9}$$

Here, C_{TOFD} represents the sub-grid scale topographic factor. Equation 8 calculates this factor by filtering 30″-resolution elevation data proposed by Beljaars et al. (2004), while Equation 9 derives the sub-grid scale topographic factors through FFT analysis of 1″-resolution elevation data, utilizing the methodology introduced in this section. Compared to Equation 8, the updated Equation 9 addresses two of the three shortcomings in the original STOFD scheme by (a) directly extracting the small-scale topographic spectra from finer resolution elevation data, and (b) accounting for the heterogeneity of STOFD effects in the u and v component directions.

The sub-grid scale topographic factor σ_{flt}^2 in the original scheme is derived from the Global Multi-resolution Terrain Elevation Data (GMTED) with the horizontal resolution of 30″ (Xue et al., 2021). In the modified scheme, the sub-grid scale topographic factors $a_{2,\mathrm{WE}}$ and $a_{2,\mathrm{SN}}$ are calculated using 1″-resolution elevation data from the Advanced Spaceborne Thermal Emission and Reflection Radiometer (ASTER, Abrams et al., 2022). Figure 2 illustrates that the $C_{\mathrm{TOFD},u}$ and $C_{\mathrm{TOFD},v}$ derived from the 1″-resolution topographic data can clearly capture more details of sub-grid terrains compared to the $C_{\mathrm{TOFD},o}$ obtained through the original method. The $C_{\mathrm{TOFD},u}$ and $C_{\mathrm{TOFD},v}$ exhibit a symmetric distribution overall, with their distributions becoming more dispersed as STOFD intensifies (Figure 2f). Therefore, it is necessary to account for the heterogeneity of STOFD in the u and v directions.

3. Data, Experimental Design, and Methodology

3.1. Data

Data for driving the RegCM4: The 6-hourly ERA-Interim reanalysis (Dee et al., 2011) with a horizontal resolution of 1.5° and 37 vertical levels and the weekly NOAA OISST data (Reynolds et al., 2002) with a horizontal resolution of 1° provide the forcing data.

Topography elevation data: The GMTED data provide the grid-scale topography elevation for the RegCM4 and the sub-grid small-scale topographic filtering variance for the original STOFD scheme. The ASTER GDEM data (Version 3, Abrams et al., 2022) offers the sub-grid scale topographic factors for the modified STOFD scheme.

Data for evaluation: The hourly precipitation is provided by the Global multi-source Merging-and-Calibration Precipitation (GMCP) data sets with a horizontal resolution of 0.1° (Ma et al., 2025). The atmospheric

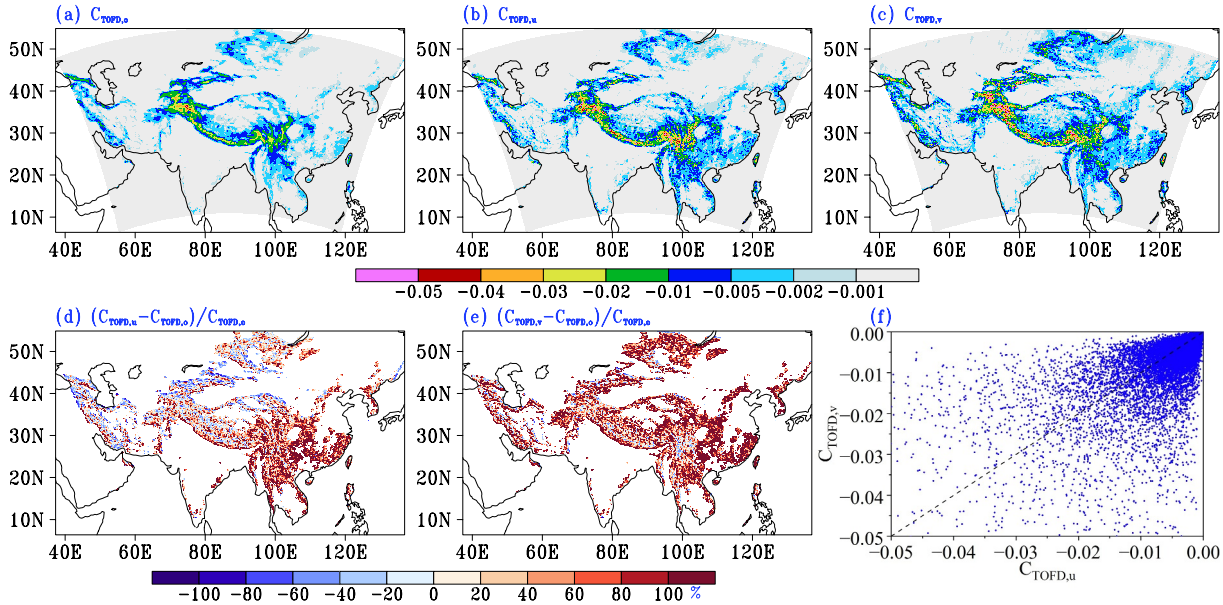

Figure 2. Sub-grid scale topographic factor at the model grids with the horizontal resolution of 25 km. (a) $C_{TOFD,o}$, (b) $C_{TOFD,u}$, (c) $C_{TOFD,v}$, (d) the relative difference between the absolute values of $C_{TOFD,u}$ and $C_{TOFD,o}$, (e) the relative difference between the absolute values of $C_{TOFD,v}$ and $C_{TOFD,o}$, and (f) scatter plot of $C_{TOFD,u}$ and $C_{TOFD,v}$.

circulation information is offered by the daily ERA5 reanalysis with a horizontal resolution of 0.25° at 37 vertical levels (Hersbach et al., 2020).

3.2. Experimental Design

The STOFD scheme was integrated into the Holtslag planetary boundary layer scheme (Holtslag et al., 1990) in RegCM4. Based on Equations 7 and 8 or Equations 7 and 9, the STOFD is incorporated into the momentum equations at all model levels. To evaluate the effects of the original and modified STOFD schemes on the simulation performance of RegCM4 over the TP, three numerical experiments were designed. The CTRL experiment employed the standard RegCM4 configuration without considering the STOFD. The SEXPO experiment implemented the original STOFD scheme developed based on low-resolution elevation data with a horizontal resolution of ∼1 km, whereas the SEXPN experiment incorporated the modified STOFD scheme updated based on high-resolution topographic data with a horizontal resolution of ∼30 m. The only difference among the three experiments is the method used to treat the STOFD. The other model configurations are identical: the Tiedtke and Kain–Fritsch cumulus convection schemes were adopted over the land and ocean, respectively (Kain, 2004; Tiedtke, 1996); the static dynamic core, the CCM3 radiative transfer scheme, the Community Land Model version 4.5, the SUBEX moisture scheme, and the Zeng ocean flux scheme were also employed (Grell et al., 1994; Kiehl et al., 1998; Oleson et al., 2013; Pal et al., 2000; Zeng et al., 1998).

Following the model configuration of Zhou et al. (2018), the simulation domain (Figure 3) covers the extensive TP and its surrounding areas to minimize the influence of lateral boundary conditions on atmospheric flow over the plateau. The model is configured with a horizontal resolution of 25 km, centered at (87°E, 33°N), and consists of 300 and 200 grids in the east-west and north-south directions, respectively. Vertically, the domain is discretized into 29 layers, extending up to 50 hPa. The simulation period was set from 00:00 UTC on 1 November of each year to 00:00 UTC on 1 March of the following year, covering the winters from 2008 to 2012. Surface variables were output hourly, while atmospheric variables were output every three hours. The analysis focused on the December-February period.

3.3. Metrics

The metrics such as the root mean square error (RMSE), spatial correlation coefficient (SC), and Taylor score (TS) (Taylor, 2001) are used to evaluate the model performance (Equations 10–13).

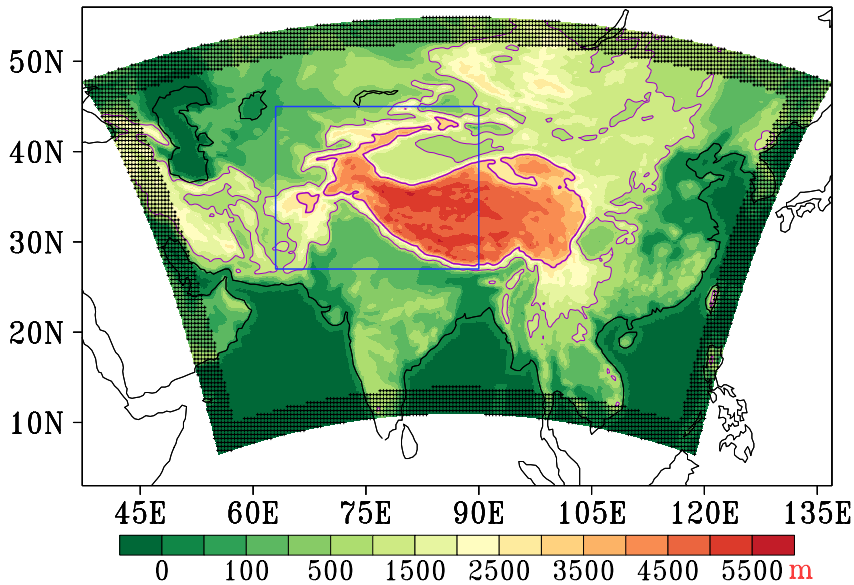

Figure 3. The elevation of grid scale topography in the model domain. The black grids in the domain boundary show the lateral boundary buffer zone. The blue rectangle is the analysis zone. The thin and thick purple lines indicate the elevations of 1,000 and 3,000 m, respectively.

$$\mathrm{RMSE} = \sqrt{\frac{\sum_{i=1}^{n}(S_i - O_i)^2}{n}} \tag{10}$$

$$\mathrm{SC} = \frac{\sqrt{\sum_{i=1}^{n}(O_i - \overline{O})(S_i - \overline{S})}}{\sqrt{\sum_{i=1}^{n}(O_i - \overline{O})^2 \sum_{i=1}^{n}(S_i - \overline{S})^2}} \tag{11}$$

$$\mathrm{TS} = \frac{4(1 + SC)}{(\gamma + 1/\gamma)^2 (1 + SC_0)} \tag{12}$$

$$\gamma = \frac{\sqrt{\frac{1}{n}\sum_{i=1}^{n}(S_i - \overline{S})^2}}{\sqrt{\frac{1}{n}\sum_{i=1}^{n}(O_i - \overline{O})^2}} \tag{13}$$

Where S and O are the simulations and observations, respectively. $\overline{S}$ ($\overline{O}$) is the mean value of simulations (observations) with a sample size of n. RMSE measures the simulation error, low RMSE suggests the simulations closely agree with the observations in quantity. SC is the spatial correlation coefficient. High SC implies high similarity in spatial variation between observations and simulations. SC_0 in Equation 12 is an achievable maximum correlation, it is set to 1. γ is calculated as the ratio of the standard deviation of the simulations to that of the observations. TS quantifies the similarity of the spatial heterogeneity between simulations and observations. Both TS and SC range from 0 to 1. Higher TS and SC and lower RMSE indicate better model performance (Huang et al., 2016).

To further clarify the impacts of the STOFD scheme on the winter precipitation simulations, this study analyzes water vapor transport $\vec{Q}$ (Equation 14) and the water vapor budget (Equation 15) using the simulation results.

$$\vec{Q} = \frac{1}{g}\int_{p_s}^{p_t} q\overrightarrow{V_h}\, dp \tag{14}$$

$$P = <\frac{\partial q}{\partial t}> + <\nabla_h \cdot (q\overrightarrow{V_h})> + <\frac{\partial(\omega q)}{\partial p}> + E + \delta \tag{15}$$

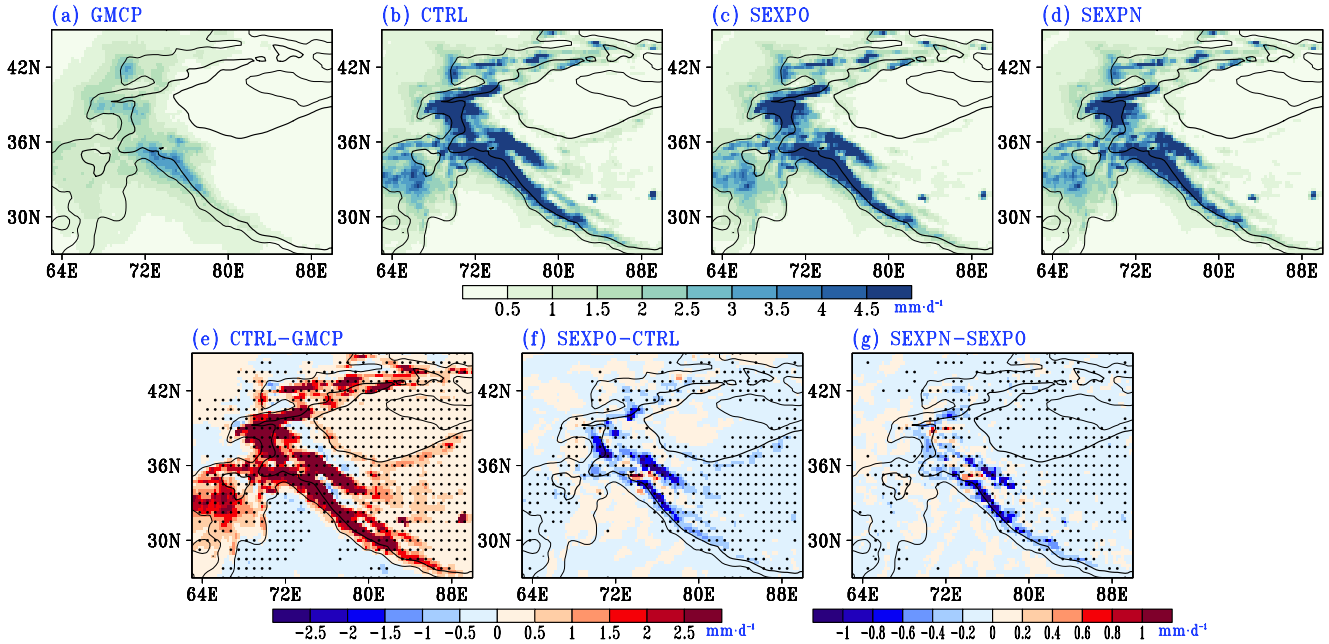

Figure 4. The observed and simulated winter precipitation over the Western TP averaged over 2008–2012: (a) the GMCP, (b) the CTRL experiment, (c) the SEXPO experiment, and (d) the SEXPN experiment. AS well as the differences of the winter precipitation (e) between the CTRL experiment and the GMCP, (f) between the SEXPO and CTRL experiments, and (g) between the SEXPN and SEXPO experiments. The thick and thin contours indicate the elevations of 3,000 and 1,000 m, respectively. The black dots in figures (e–g) show the differences passing the t-student test with a significance of 95%.

Where g, p_t, p_s, p, P, q, t, $\overrightarrow{V_h}$, ω, E, and δ are the gravity acceleration, surface pressure, pressure of top layer, pressure of each layer, precipitation rate, specific humility, time, horizontal wind, vertical velocity, evaporation rate, and residual, respectively. The operators ∇_h and $< >$ are $\nabla_h = \frac{\partial}{\partial x} + \frac{\partial}{\partial y}$ and $< >= -\frac{1}{g}\int_{p_s}^{p_t} dp$, respectively. p_t is set as 100 hPa in this study. The terms $<\frac{\partial q}{\partial t}>$, $<\nabla_h \cdot (q\overrightarrow{V_h})>$, and $<\frac{\partial(\omega q)}{\partial p}>$ represent the local moisture tendency, horizontal moisture convergence, and vertical moisture transport, respectively. The detailed derivation and explanation of Equation 15 can be found in Seager et al. (2010), Cai et al. (2023), and Xu et al. (2024).

4. Model Evaluation

The observed winter precipitation in western TP is largely confined to elevations below 3,000 m, with maximum values occurring between 1,000 and 3,000 m in the western Himalayas (Figure 4a). The CTRL experiment without considering the STOFD exhibits a pronounced positive bias in the simulated winter precipitation over this region (Figures 4b and 4e). Although the CTRL experiment can well capture the spatial distribution of precipitation over western TP and its surrounding areas, it produces spurious precipitation above 3,000 m (Figure 4e). The SEXPO experiment adopting the original STOFD scheme partially reduced the overestimation of the simulated precipitation in the CTRL experiment (Figures 4e and 4f). However, it does not fully eliminate the excessive winter precipitation in the western TP simulated by the CTRL experiment (Figures 4a and 4c). In contrast, the SEXPN experiment adopting the updated STOFD scheme further suppressed the overestimation of winter precipitation in the western TP more effectively than the SEXPO experiment (Figures 4f and 4g).

The implementation of the STOFD schemes leads to clear improvements in the simulation of winter precipitation over the western TP, evidenced by higher SC and TS, as well as a markedly reduced RMSE (Figure 5). Specifically, the SEXPO experiment produces increases of 2.6% in SC and 17.5% in TS, along with a 16.3% reduction in RMSE, relative to the CTRL experiment. Comparison of the SEXPN and SEXPO experiments indicates that adopting the modified STOFD scheme can lead to additional improvements in simulated winter precipitation, with SC and TS increased by 1.3% and 6.4%, respectively, and the RMSE reduced by 6.3% (Figures 5d–5f). These quantitative results demonstrate that adopting each of the original and modified STOFD schemes can clearly enhance the model performance in simulating winter precipitation over the western TP, with the modified one performing better than the original one.

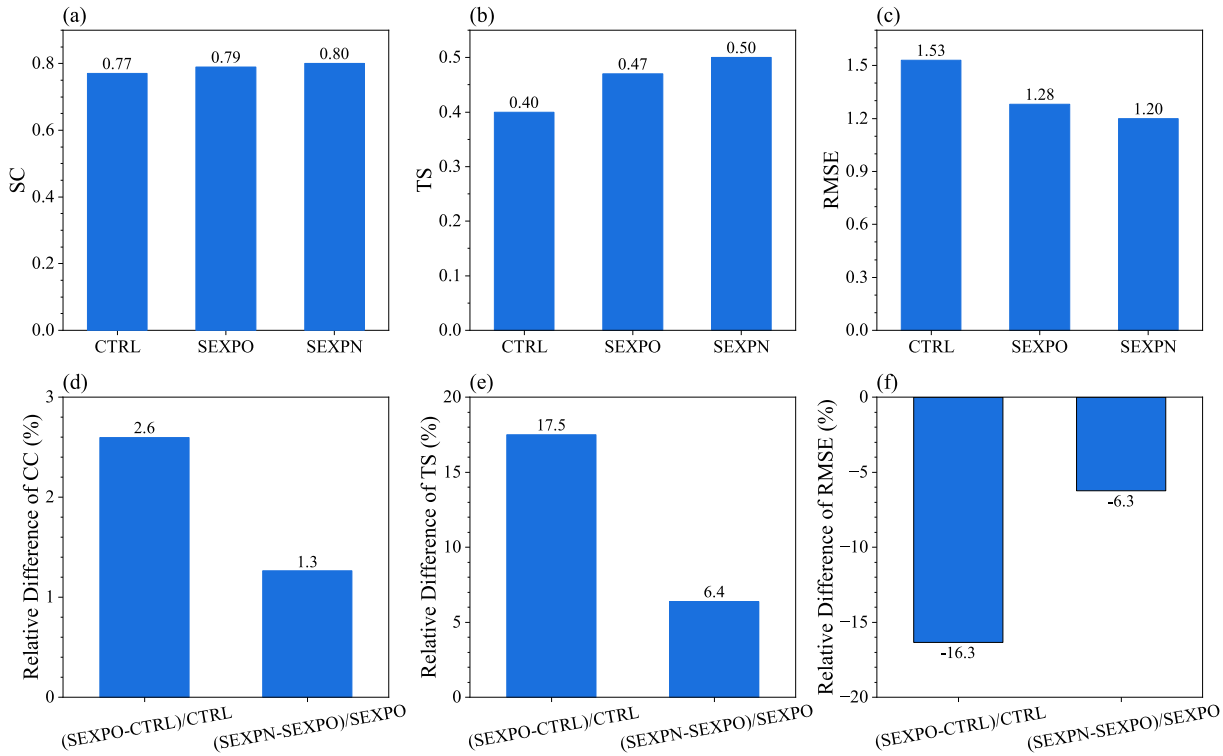

Figure 5. The (a) Spatial correlation (SC), (b) Taylor score (TS), and (c) root mean square error (RMSE) of the simulated climatic mean winter precipitation over the Western TP during 2008–2012, along with the relative differences (d–f) in these metrics between the experiments are presented. The statistics were calculated over the grid points within the blue rectangle shown in Figure 3.

5. Possible Physical Mechanisms

The CTRL without considering the STOFD clearly overestimates the 10 m wind speed over complex terrains, especially over the regions with elevations above 3,000 m where the 10 m wind speed is overestimated by more than 5 $m \cdot s^{-1}$ (Figures 6a, 6b, and 6e). Adopting the original STOFD scheme can substantially reduce this near-surface wind speed bias (Figures 6c and 6f), and adopting the modified STOFD scheme achieves an even greater reduction (Figures 6d and 6g). At 500 hPa, the CTRL experiment overestimates the wind speed over the TP in winter but underestimates the jet stream speeds along its northern and southern flanks (Figures 6h, 6i, and 6l). Adoption of the original STOFD scheme mitigates both the mid-tropospheric overestimation of wind speed over the plateau and the underestimation of wind speed in the jet regions (Figures 6j and 6m), leading to an overall improvement in the 500 hPa wind simulation. Adopting the modified STOFD scheme yields further improvement (Figures 6k and 6n). The reduction in wind speed bias is attributed to a drag generated by the STOFD scheme, which acts opposite to the flow direction (red vectors in Figures 6c, 6d, 6j, and 6k). The modified scheme produces stronger drag (purple vectors in Figures 6d and 6k) due to its more accurate representation of sub-grid scale topographic variations, explaining its superior performance in correcting the wind speed overestimation. Adopting the STOFD scheme consistently improves the simulation of winds at both 10 m and 500 hPa levels in winter, and adoption of the modified one can yield more improvement.

The spatial pattern of differences in the simulated vertical velocity at 500 hPa between the CTRL experiment and ERA5 aligns with major topographic features (Figure 7a). Over mountain ranges such as the Kunlun, Karakoram, and Himalayas, the CTRL experiment simulates excessively strong upward motion, while the intermontane regions exhibit overly weak ascent. From Figures 7a and 7b, adopting the original STOFD scheme can reduce the overestimation (underestimation) of simulated upward motion at 500 hPa over the major mountain ranges (intermontane areas) in the CTRL experiment, leading to an overall improvement in the 500 hPa vertical velocity simulation. The SEXPN experiment adopting the modified STOFD scheme can further improve the simulation of vertical motion at 500 hPa (Figures 7b and 7c). The differences in vertical motion are caused by variations in horizontal wind speed, which can be explained as follows: higher wind speeds correspond to greater horizontal

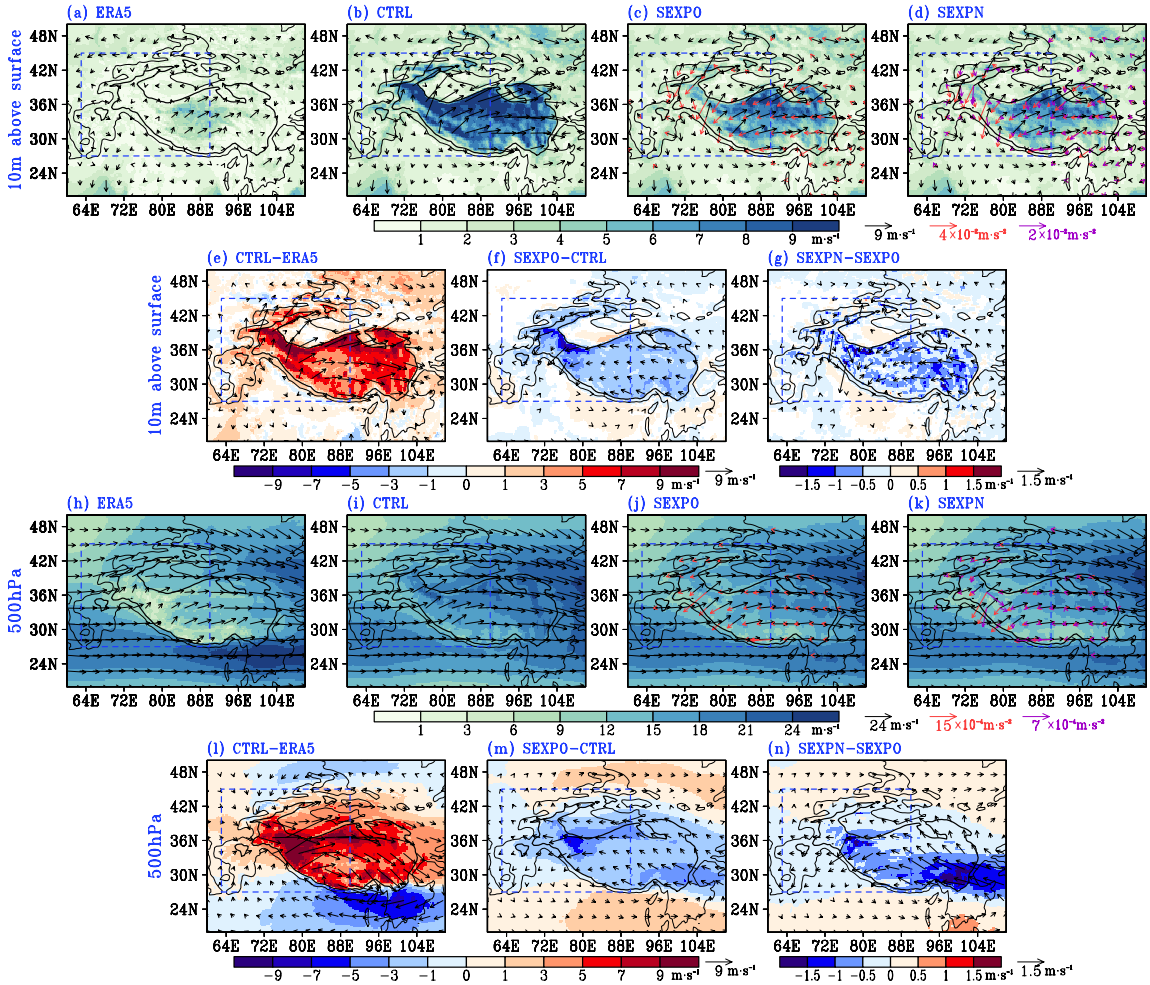

Figure 6. The climatic mean winter wind speed at 10 m and 500 hPa in the Western TP over 2008–2012: ERA5 reanalysis (a, h) and the simulations from different experiments (b–d, i–k). The differences in the winter wind among the ERA5 reanalysis and the simulations from different experiments (e–g, l–n). The red vectors show the STOFD from the SEXPO and SEXPN experiments. The purple vectors represent the differences in the STOFD between the SEXPN and SEXPO experiments. The black vectors indicate the wind or the difference in wind. The thick and thin contours indicate the elevations of 3,000 and 1,000 m, respectively. Differences in wind speed that are not above the 95% significance level in the *t*-test have been masked out.

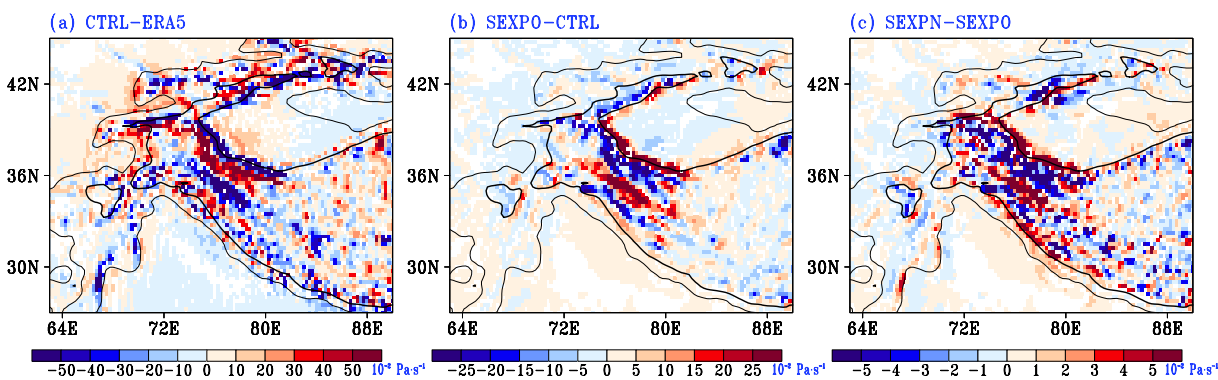

Figure 7. The differences in the climatic mean vertical velocity at the 500 hPa in winter over 2008–2012 are (a) between the CTRL experiment and ERA5, (b) the SEXPO experiment and CTRL experiment, and (c) between SEXPN experiment and SEXPO experiment. Vertical velocity differences that are not above the 95% significance level in the *t*-test have been masked out. The thick and thin contours indicate the elevations of 3,000 and 1,000 m, respectively. The negative vertical velocity indicates upward motion.

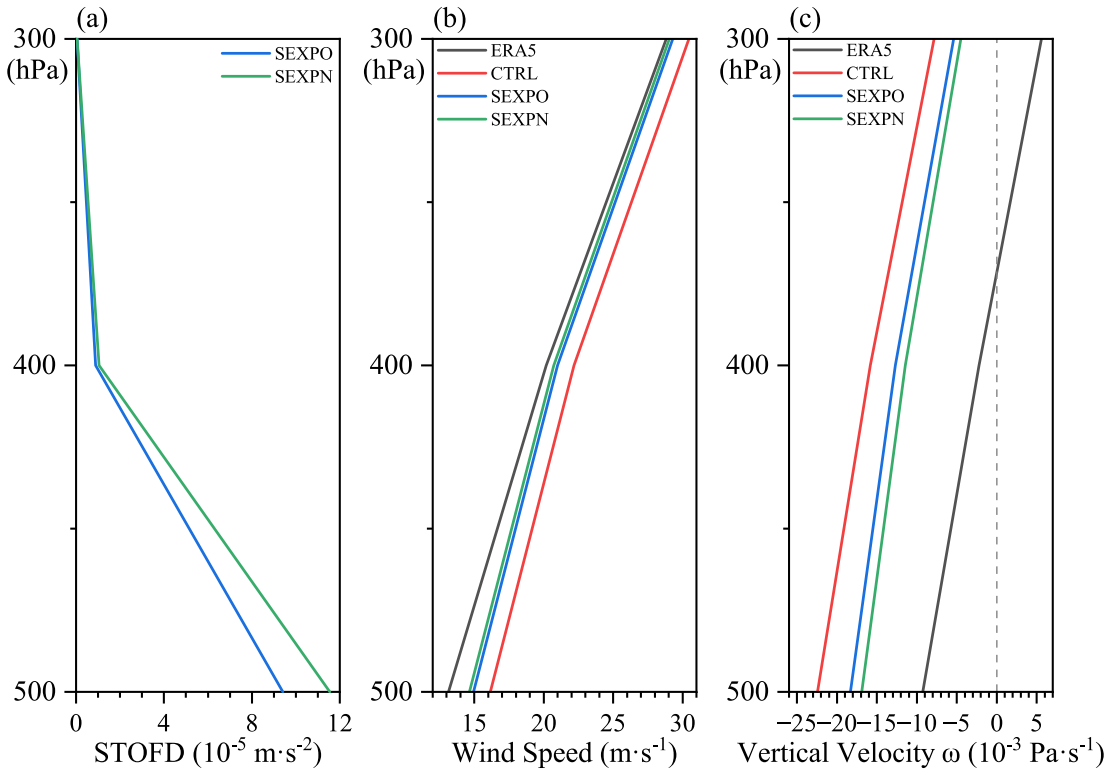

Figure 8. Vertical profiles of regionally averaged STOFD (a), horizontal wind speed (b), and vertical velocity (c) over the western TP indicated by the blue rectangle in Figure 3 simulated by each experiment during the winters of 2008–2012. The negative vertical velocity indicates upward motion.

momentum when mass remains constant. The total momentum of the airflow is the sum of its horizontal and vertical components. When air flows over a mountain, the meso-scale terrain's blocking effect converts part of the horizontal momentum into vertical momentum, resulting in upward motion on the windward slope and downward motion on the leeward slope. Therefore, a larger horizontal wind speed produces greater initial momentum and, consequently, higher vertical velocity. As a result, the CTRL simulation, which exhibits significantly higher horizontal wind speeds than the ERA5 data, also produces stronger vertical motions (Figures 6l and 7a). This is evident in the more intense upward motion on the windward slopes and stronger downward motion on the leeward slopes (Figure 7a). When the both STOFD schemes are applied, the simulated horizontal wind speed decreases (Figures 6m and 6n), and the corresponding upward and downward motions on the windward and leeward slopes are suppressed (Figures 7b and 7c).

The STOFD decreases exponentially with height over the western TP, diminishing to near zero at around 300 hPa (Figure 8a). Although the modified STOFD scheme produces stronger near-surface drag than the original one, the difference between them decreases markedly with altitude. The CTRL experiment significantly overestimates both the horizontal wind speed and vertical velocity between 500 and 300 hPa over the western TP compared to the ERA5 reanalysis (Figures 8b and 8c). The implementation of the STOFD scheme can clearly reduce these biases across the regions. Adopting the modified STOFD scheme can further achieve a greater reduction in the overestimation of both wind speed and vertical velocity between 500 and 300 hPa over the western TP relative to the original STOFD scheme.

Overall, introducing the STOFD scheme (notably the modified scheme) can significantly improve the simulation of horizontal winds and vertical velocity structure across complex terrains of western TP in winter (Figures 6–8). It is worth noting that, although the suppression of upward motion on the windward slope and downward motion on the leeward slope are comparable after applying the STOFD scheme (Figures 7b and 7c), the reduction in precipitation on the windward slope is significantly more pronounced than the increase on the leeward slope (Figures 4f and 4g). The reason is that, after implementing the STOFD scheme, the simulated water vapor transport across the entire region is significantly reduced and more accurate due to the improved simulation of the

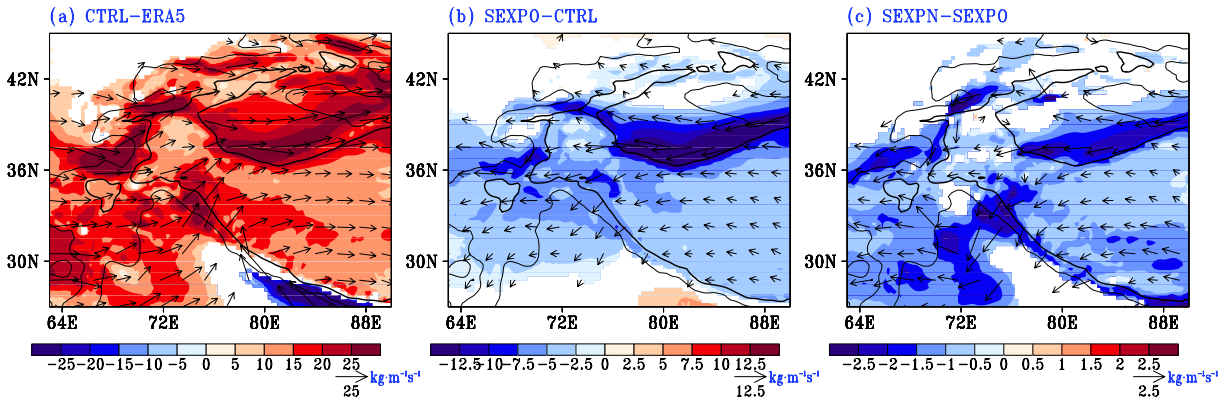

Figure 9. The differences in the climatic mean water vapor transport flux integrated from the surface to 100 hPa over the winters of 2008–2012: (a) between the CTRL experiment and ERA5, (b) between the SEXPO experiment and CTRL experiment, and (c) between the SEXPN experiment and SEXPO experiment. Differences that are not above the 95% significance level in the *t*-test have been masked out. The thick and thin contours indicate the elevations of 3,000 m and 1,000 m, respectively.

wind fields (Figure 9). The CTRL experiment clearly overestimates the moisture transport flux over the western TP, with the maximum bias exceeding 25 kg m^{-1} s^{-1} along the TP-Tarim Basin boundary (Figure 9a). Adopting the original STOFD scheme can lead to this bias significantly reduced by up to 12.5 kg m^{-1} s^{-1} (Figure 9b). A further reduction of bias can be achieved by adopting the modified STOFD scheme, leading to a more accurate simulation of moisture transport than the original one (Figure 9c). Precipitation formation requires three fundamental elements: water vapor, upward motion (which provides cooling and condensation conditions), and cloud condensation nuclei. Consequently, the distribution of reduced water vapor transport shown in Figure 9 does not exactly correspond to the distribution of reduced precipitation in Figure 4. For example, the region with the most pronounced reduction in water vapor transport is the Taklamakan Desert, located north of the TP. This area is dominated by subsiding airflow, which inhibits precipitation formation. Therefore, although the STOFD scheme weakens the simulated winter water vapor transport across the entire western TP, its impact on winter precipitation remains limited to the regions where precipitation originally occurred.

Compared to ERA5, the regional mean components of the moisture budget over the western TP are systematically overestimated by the CTRL experiment (Figure 10). The SEXPO and SEXPN experiments considering the STOFD can clearly reduce these biases across multiple moisture budget components relative to the CTRL experiment without the STOFD (Figure 10). Obviously, compared to the CTRL experiment, the reduced simulation of winter precipitation over the western TP in both STOFD-based experiments is primarily attributable to the reduction of the simulations of local moisture tendency and horizontal moisture convergence, which lead to the improved simulations of winter precipitation over the western TP. The reduction in the simulated local moisture tendency is a feedback response to the decreased precipitation and evaporation, while the decrease in the simulated horizontal moisture convergence is a direct result of the altered horizontal wind field.

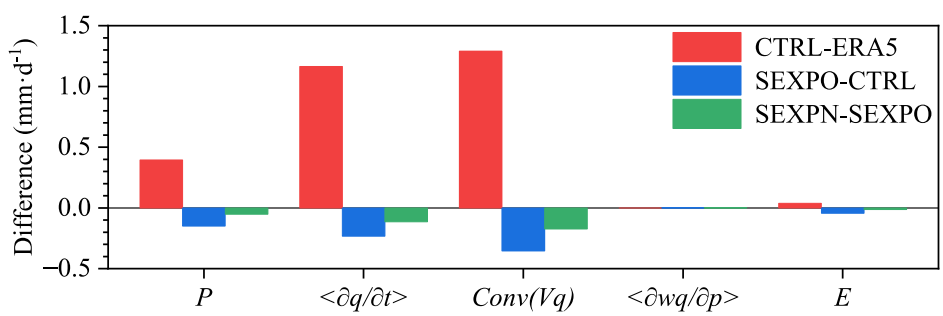

Figure 10. Differences in each moisture budget component regionally averaged over the western TP indicated by the blue rectangle in Figure 3 between the simulations of CTRL experiment and ERA5 and among the simulations of different experiments during the winters of 2008–2012. The terms P, <∂*q*/∂*t*>, Conv(*Vq*), <∂wq/∂*p*>, and E represent the precipitation rate, local moisture tendency, horizontal moisture convergence, vertical moisture transport, and evaporation rate, respectively.

Overall, the primary reason for the suppressed wet bias in RegCM4's simulation of precipitation (Figures 4 and 5) over the western TP, when using the STOFD scheme, is the reduction of simulated vertical motion and the weakening of water vapor transport across the entire region (Figures 7 and 9). Fundamentally, this is caused by the weakening of the atmospheric westerly flow due to the STOFD scheme (Figures 6 and 8). After considering the STOFD scheme, the significant reduction in precipitation on the windward slope is attributed to the combined effects of anomalous downward motion and negative water vapor transport anomalies. Conversely, changes in precipitation simulation on the leeward slope are not significant, as they result from the mutually offsetting effects of anomalous upward motion and negative water vapor transport anomalies.

6. Conclusion and Discussion

The STOFD associated with sub-grid small-scale terrain features remains inadequately represented in numerical models. The classic Beljaars STOFD scheme suffers from limitations such as being developed based on low-resolution elevation data and the assumption of isotropic drag. This study refines the Beljaars scheme by deriving anisotropic topographic factors from high-resolution (~30 m) elevation data. We implemented both the original and modified STOFD schemes into RegCM4 and conducted three numerical experiments: a control run (CTRL) without STOFD, one with the original scheme (SEXPO), and another with the modified scheme (SEXPN). Based on these experiments, we systematically evaluate how each scheme affects the simulation of winter precipitation over the western TP and investigate the underlying physical mechanisms. The key findings are summarized as follows:

RegCM4 without considering the STOFD significantly overestimates the winter precipitation over the western TP. Adopting each of the original and modified STOFD schemes can effectively reduce this overestimation of winter precipitation over western TP. Relative to the CTRL experiment, the SEXPO experiment adopting the original STOFD can lead to the SC and TS (RMSE) of simulated winter precipitation over the western TP increased by 2.6% and 17.5% (reduced by 16.3%), respectively. Moreover, compared to the SEXPO experiment, the SEXPN experiment adopting the modified STOFD scheme can further increase (reduce) the CC and TS (RMSE) of simulated winter precipitation over the western TP by 1.3% and 6.4% (6.3%), respectively.

The introduction of STOFD, which acts opposite to the flow direction, can effectively reduce the overestimation of 10 m wind speeds over the complex terrains of TP. This correction can extend to the 500 hPa level, where the STOFD schemes mitigate the overestimation of wind over the plateau itself and the underestimation of jet stream speeds on its flanks. Consequently, the excessive 500 hPa upward motion over major ranges (e.g., Kunlun, Karakoram, Himalayas) is weakened while the 500 hPa ascent over intermountain areas is enhanced, leading to a more realistic 500 hPa vertical velocity simulations. Moreover, relative to the original STOFD scheme, the modified STFOD scheme producing consistently stronger drag leads to further improvements in all aspects mentioned above.

Relative to the situations without the STOFD, the improvements in wind field simulations induced by the STOFD lead to a more realistic representation of moisture transport. Adopting each of the original and modified STOFD schemes substantially reduces the overestimation of moisture transport over the western TP produced in the CTRL experiment without STOFD, with much more improvements in the moisture transport simulation induced by the modified STOFD scheme. Consequently, the overestimation of local moisture tendency and horizontal moisture convergence over the western TP in the CTRL experiment during winter is reduced by adopting each of the original and modified STOFD schemes, further leading to the improved simulations of winter precipitation over the western TP with much more obvious improvement induced by the modified STOFD scheme than the original one.

The impact of the STOFD scheme on the precipitation simulation performance varies between windward and leeward slopes. The simulated precipitation on the windward slope decreases significantly due to the combined effects of anomalous downward motion and negative water vapor transport anomalies. In contrast, changes in the simulated precipitation on the leeward slope are not significant because they result from the mutually offsetting influences of anomalous upward motion and negative water vapor transport anomalies.

Overall, this study demonstrates that incorporating the STOFD scheme including the anisotropic topographic factors clearly improves the performance of RegCM4 over complex terrains of the western TP. Our results confirm the important role of STOFD in regional climate modeling, particularly over rugged regions such as the

western TP. Although the original STOFD scheme effectively reduces the simulation biases of precipitation and wind speed over western TP in winter, the improvement is limited by insufficient representation of fine-scale topographic features. The modified STOFD scheme addresses this limitation by employing high-resolution (∼30 m) elevation data to compute direction-dependent drag forces (applying distinct STOFD to u and v wind components), thereby more accurately capturing the drag effects of complex topography. This enhancement yields additional improvements in simulations of wind fields, vertical motion, moisture transport, and thereafter precipitation. This study also highlights the importance of using high-resolution topographic data to represent the STOFD in numerical models.

Nevertheless, this study has certain limitations. First, despite substantial improvements, residual biases persist in specific regions, such as the areas along the western margins of the TP (e.g., persistent overestimation of moisture transport). These may be attributed to physical processes not fully captured in RegCM4, such as orographic gravity wave drag. Second, the influence of the STOFD schemes on simulations of other climatic variables, such as near-surface temperature and snow cover, and their performance beyond the winter season require further assessment. Future work should address these aspects to achieve a more comprehensive understanding.

Conflict of Interest

The authors declare no conflicts of interest relevant to this study.

Availability Statement

Data: This research utilize the daily precipitation data from the GMCP dataset (Ma, 2025), the hourly ERA-Interim reanalysis (ECMWF, 2011), the hourly ERA5 reanalysis data (ECMWF, 2018), the elevation from the Aster GDEM dataset (ASTER Science Team, 2019) and the GMTED data (Danielson & Gesch, 2011), and the weekly NOAA OISST (NOAA, 2002). *Software*: The base version of RegCM4 was obtained from ICTP. The complete source code, which includes the original RegCM4 as well as RegCM4 implementations with both the original and modified STOFD parameterization schemes, is available from Gu and Huang (2026).

Acknowledgments
This research was financially supported by the National Natural Science Foundation of China (Grant 42375157). We also appreciate for the support by the Jiangsu Collaborative Innovation Center for Climate Change, and the China Postdoctoral Science Foundation under Grant 2025M780281. We thank the High Performance Computing Center of Nanjing University for offering the computing resources. We sincerely thank the editor and reviewers for their constructive comments, which have significantly improved the quality of the manuscript.

References

Abrams, M., Yamaguchi, Y., & Crippen, R. (2022). ASTER global DEM (GDEM) version 3. *The International Archives of the Photogrammetry, Remote Sensing and Spatial Information Sciences*, *XLIII-B4–2022*, 593–598. https://doi.org/10.5194/isprs-archives-XLIII-B4-2022-593-2022

ASTER Science Team. (2019). ASTER global digital elevation model V003 [Dataset]. *NASA Land Processes Distributed Active Archive Center*. https://doi.org/10.5067/ASTER/ASTGTM.003

Bannon, P., & Yuhas, J. (1990). On Mountain wave drag over complex terrain. *Meteorology and Atmospheric Physics*, *43*(1–4), 155–162. https://doi.org/10.1007/Bf01028118

Bao, Q., & Li, J. (2020). Progress in climate modeling of precipitation over the Tibetan Plateau. *National Science Review*, *7*(3), 486–487. https://doi.org/10.1093/nsr/nwaa006

Beljaars, A. C. M., Brown, A. R., & Wood, N. (2004). A new parametrization of turbulent orographic form drag. *Quarterly Journal of the Royal Meteorological Society*, *130*(599), 1327–1347. https://doi.org/10.1256/qj.03.73

Cai, S., Huang, A., Zhu, K., Guo, W., Wu, Y., & Gu, C. (2023). The forecast skill of the summer precipitation over Tibetan Plateau improved by the adoption of a 3D sub-grid terrain solar radiative effect scheme in a convection-permitting model. *Journal of Geophysical Research: Atmospheres*, *128*(11), e2022JD038105. https://doi.org/10.1029/2022JD038105

Cui, T., Li, C., & Tian, F. (2021). Evaluation of temperature and precipitation simulations in CMIP6 models over the Tibetan Plateau. *Earth and Space Science*, *8*(7), e2020EA001620. https://doi.org/10.1029/2020EA001620

Curio, J., & Scherer, D. (2016). Seasonality and spatial variability of dynamic precipitation controls on the Tibetan Plateau. *Earth System Dynamics*, *7*(3), 767–782. https://doi.org/10.5194/esd-7-767-2016

Danielson, J. J., & Gesch, D. B. (2011). Global multi-resolution terrain elevation data 2010 (GMTED2010) [Dataset]. *Open-File Report*. https://doi.org/10.3133/ofr20111073

Dee, D. P., Uppala, S. M., Simmons, A. J., Berrisford, P., Poli, P., Kobayashi, S., et al. (2011). The ERA-interim reanalysis: Configuration and performance of the data assimilation system. *Quarterly Journal of the Royal Meteorological Society*, *137*(656), 553–597. https://doi.org/10.1002/qj.828

ECMWF. (2011). The ECMWF reanalysis-interim (ERA-Interim) [Dataset]. https://doi.org/10.5065/D6CR5RD9

ECMWF. (2018). The fifth-generation ECMWF atmospheric reanalysis (ERA5) [Dataset]. https://doi.org/10.24381/cds.adbb2d47

Emeis, S., & Zilitinkevich, S. (1991). Resistance law, effective roughness length, and deviation angle over hilly terrain. *Boundary-Layer Meteorology*, *55*(1), 191–198. https://doi.org/10.1007/BF00119334

Farr, T., Rosen, P., Caro, E., Caro, E., Crippen, R., Duren, R., et al. (2008). The shuttle radar topography mission. *Reviews of Geophysics*, *45*(2), RG2004. https://doi.org/10.1029/2005RG000183

Fiedler, F., & Panofsky, H. (1972). The geostrophic drag coefficient and the "effective" roughness length. *Quarterly Journal of the Royal Meteorological Society*, *98*(415), 213–220. https://doi.org/10.1002/qj.49709841519

Fu, Y., Gao, X., Zhu, Y., & Guo, D. (2021). Climate change projection over the Tibetan Plateau based on a set of RCM simulations. *Advances in Climate Change Research*, *12*(3), 313–321. https://doi.org/10.1016/j.accre.2021.01.004

Fujisada, H., Urai, M., & Iwasaki, A. (2012). Technical methodology for ASTER global DEM. *IEEE Transactions on Geoscience and Remote Sensing*, *50*(10), 3725–3736. https://doi.org/10.1109/TGRS.2012.2187300

Gao, X., & Giorgi, F. (2017). Use of the RegCM system over East Asia: Review and perspectives. *Engineering*, *3*(5), 766–772. https://doi.org/10.1016/J.ENG.2017.05.019

Gao, X., Shi, Y., Han, Z., Wang, M., Wu, J., Zhang, D., et al. (2017). Performance of RegCM4 over major river basins in China. *Advances in Atmospheric Sciences*, *34*(4), 441–455. https://doi.org/10.1007/s00376-016-6179-7

Grell, G., Dudhia, J., & Stauffer, D. (1994). Description of the fifth generation Penn State/NCAR Mesoscale Model (MM5). *Tech. Rep. TN-398+STR, NCAR*.

Grohmann, C. (2018). Evaluation of TanDEM-X DEMs on selected Brazilian sites: Comparison with SRTM, ASTER GDEM and ALOS AW3D30. *Remote Sensing of Environment*, *212*, 121–133. https://doi.org/10.1016/j.rse.2018.04.043

Gu, C., & Huang, A. (2026). Source code for RegCM-4.5.0 with the original and revised sub-grid turbulent orographic form drag schemes [Software]. *Zenodo*. https://doi.org/10.5281/zenodo.19159340

Gu, C., Huang, A., Li, X., & Wu, Y. (2024). The cold bias in the surface air temperature simulations over the Tibetan Plateau of RegCM4 reduced by adopting the 3D sub-grid terrain longwave radiative effect scheme. *Journal of Geophysical Research: Atmospheres*, *129*(23), e2024JD042102. https://doi.org/10.1029/2024JD042102

Gu, C., Huang, A., Li, X., Yang, B., Zhou, X., & Wu, Y. (2023). Impact of sub-grid turbulent orographic form drag on the summer monsoon precipitation simulation over China. *Journal of Geophysical Research: Atmospheres*, *128*(20), e2023JD039113. https://doi.org/10.1029/2023JD039113

Gu, C., Huang, A., Zhang, Y., Yang, B., Cai, S., Xu, X., et al. (2022). The wet bias of RegCM4 over Tibet Plateau in summer reduced by adopting the 3D sub-grid terrain solar radiative effect parameterization scheme. *Journal of Geophysical Research: Atmospheres*, *127*(21), e2022JD037434. https://doi.org/10.1029/2022JD037434

Gu, H., Yu, Z., Peltier, W. R., & Wang, X. (2020). Sensitivity studies and comprehensive evaluation of RegCM4.6.1 high-resolution climate simulations over the Tibetan Plateau. *Climate Dynamics*, *54*(7), 3781–3801. https://doi.org/10.1007/s00382-020-05205-6

Guo, D., Sun, J., & Yu, E. (2018). Evaluation of CORDEX regional climate models in simulating temperature and precipitation over the Tibetan Plateau. *Atmospheric and Oceanic Science Letters*, *11*(3), 219–227. https://doi.org/10.1080/16742834.2018.1451725

Hersbach, H., Bell, B., Berrisford, P., Biavati, G., Horányi, A., Muñoz-Sabater, J., et al. (2020). The ERA5 global reanalysis. *Quarterly Journal of the Royal Meteorological Society*, *146*(730), 1999–2049. https://doi.org/10.1002/qj.3803

Holtslag, A., De Bruijn, E., & Pan, H. (1990). A high resolution air mass transformation model for short-range weather forecasting. *Monthly Weather Review*, *118*(8), 1561–1575. https://doi.org/10.1175/1520-0493(1990)118<1561:ahramt>2.0.co;2;2

Hu, Q., Hua, W., Yang, K., Ming, J., Ma, P., Zhao, Y., & Fan, G. (2022). An assessment of temperature simulations by CMIP6 climate models over the Tibetan Plateau and differences with CMIP5 climate models. *Theoretical and Applied Climatology*, *148*(1), 223–236. https://doi.org/10.1007/s00704-022-03944-6

Huang, A., Zhao, Y., Zhou, Y., Yang, B., Zhang, L., Dong, X., et al. (2016). Evaluation of multisatellite precipitation products by use of groundbased data over China. *Journal of Geophysical Research-Atmospheres*, *121*(18), 10654–10675. https://doi.org/10.1002/2016JD025456

Huang, J., Zhou, X., Wu, G., Xu, X., Zhao, Q., Liu, Y., et al. (2023). Global climate impacts of land-surface and atmospheric processes over the Tibetan Plateau. *Reviews of Geophysics*, *61*(3), e2022RG000771. https://doi.org/10.1029/2022RG000771

Kain, J. (2004). The kain–fritsch convective parameterization: An update. *Journal of Applied Meteorology and Climatology*, *43*(1), 170–181. https://doi.org/10.1175/1520-0450(2004)043<0170:TKCPAU>2.0.CO;2

Karim, R., Li, S., Su, T., Ayugi, B., Babaousmail, H., & Xiao, S. (2025). Future climate changes on the Qinghai–Tibetan Plateau under CMIP6 global climate models. *International Journal of Climatology*, *45*(11), e70005. https://doi.org/10.1002/joc.70005

Kiehl, J., Hack, J., Bonan, G., Boville, B., Williamson, D., & Rasch, P. (1998). The National Center for Atmospheric Research Community Climate Model: CCM3. *Journal of Climate*, *11*(6), 1131–1149. https://doi.org/10.1175/1520-0442(1998)011<1131:tncfar>2.0.co;2;2

Koo, M., Choi, H., & Han, Y. (2018). A parameterization of turbulent-scale and mesoscale orographic drag in a global atmospheric model. *Journal of Geophysical Research-Atmospheres*, *123*(16), 8400–8417. https://doi.org/10.1029/2017jd028176

Li, D., Yang, K., Tang, W., Li, X., Zhou, X., & Guo, D. (2020). Characterizing precipitation in high altitudes of the western Tibetan Plateau with a focus on major glacier areas. *International Journal of Climatology*, *40*(12), 5114–5127. https://doi.org/10.1002/joc.6509

Li, G., Chen, H., Xu, M., Zhao, C., Zhong, L., Li, R., et al. (2022). Impacts of topographic complexity on modeling moisture transport and precipitation over the Tibetan Plateau in summer. *Advances in Atmospheric Sciences*, *39*(7), 1151–1166. https://doi.org/10.1007/s00376-022-1409-7

Li, J., Lu, C., Chen, J., Zhou, X., Yang, K., Li, J., et al. (2024). The influence of complex terrain on cloud and precipitation on the foot and slope of the southeastern Tibetan Plateau. *Climate Dynamics*, *62*(5), 3143–3163. https://doi.org/10.1007/s00382-023-07056-3

Li, P., Niu, X., Mao, Y., Wu, R., & Ling, X. (2023). Assessment of climate simulation over the Tibetan Plateau based on high-resolution multi-RCM within CORDEX-EA-II. *Atmospheric Research*, *292*, 106848. https://doi.org/10.1016/j.atmosres.2023.106848

Li, Y., Gao, Y., Chen, G., Wang, G., & Zhang, M. (2024). Decomposition and reduction of WRF-modeled wintertime cold biases over the Tibetan Plateau. *Climate Dynamics*, *62*(5), 4189–4203. https://doi.org/10.1007/s00382-024-07126-0

Lin, C., Chen, D., Yang, K., & Ou, T. (2018). Impact of model resolution on simulating the water vapor transport through the central himalayas: Implication for models' wet bias over the Tibetan Plateau. *Climate Dynamics*, *51*(9), 3195–3207. https://doi.org/10.1007/s00382-018-4074-x

Liu, J., Yang, K., Zhao, D., Wu, P., Wang, J., Zhou, X., et al. (2024). Cloud radiative feedback to the large-scale atmospheric circulation greatly reduces monsoon-season wet bias over the Tibetan Plateau in climate modeling. *Geophysical Research Letters*, *51*(14), e2024GL109180. https://doi.org/10.1029/2024GL109180

Liu, X., Liu, Y., Wang, X., & Wu, G. (2020). Large-scale dynamics and moisture sources of the precipitation over the Western Tibetan Plateau in boreal winter. *Journal of Geophysical Research: Atmospheres*, *125*(9), e2019JD032133. https://doi.org/10.1029/2019JD032133

Liu, Y., Miao, S., Liu, L., & Hu, F. (2019). Effects of a modified sub-grid-scale terrain parameterization scheme on the simulation of low-layer wind over complex terrain. *Journal of Applied Meteorological Science*, *30*(1), 70–81. https://doi.org/10.11898/1001-7313.20190107

Liu, Z., Gao, Y., & Zhang, G. (2022). How well can a convection-permitting-modelling improve the simulation of summer precipitation diurnal cycle over the Tibetan Plateau? *Climate Dynamics*, *58*(11–12), 3121–3138. https://doi.org/10.1007/s00382-021-06090-3

Lorente-Plazas, R., Jiménez, P. A., Dudhia, J., & Montávez, J. P. (2016). Evaluating and improving the impact of the atmospheric stability and orography on surface winds in the WRF model. *Monthly Weather Review*, *144*(7), 2685–2693. https://doi.org/10.1175/MWR-D-15-0449.1

Luo, J., Huang, A., Jiang, X., Xu, M., Miao, X., Gu, C., & Zhu, X. (2025). The cold biases in the soil and surface air temperature simulations of RegCM4.7 model over the Tibetan Plateau in cold seasons reduced by adopting an improved snow cover fraction scheme. *Journal of Geophysical Research: Atmospheres*, *130*(8), e2025JD043507. https://doi.org/10.1029/2025JD043507

Ma, X., Tian, L., Jiang, Y., Liang, J., Tian, J., Zhou, J., et al. (2023). Large uncertainties in precipitation exert considerable impact on land surface temperature modeling over the Tibetan Plateau. *Journal of Geophysical Research: Atmospheres*, *128*(9), e2022JD037615. https://doi.org/10.1029/2022JD037615

Ma, Y., Lu, M., Chen, H., Pan, M., & Hong, Y. (2018). Atmospheric moisture transport versus precipitation across the Tibetan Plateau: A mini-review and current challenges. *Atmospheric Research*, *209*, 50–58. https://doi.org/10.1016/j.atmosres.2018.03.015

Ma, Z. (2025). GMCP: A fully global multi-source merging-and-calibration precipitation dataset (1-hourly, 0.1°, global, 2000-Present) [Dataset]. *National Tibetan Plateau / Third Pole Environment Data Center*. https://doi.org/10.11888/Atmos.tpdc.301878

Ma, Z., Xu, J., Dong, B., Hu, X., Hu, H., Yan, S., et al. (2025). GMCP: A fully global multisource merging-and-calibration precipitation dataset (1-Hourly, 0.1, global, 2000–the present). *Bulletin of the American Meteorological Society*, *106*(4), E596–E624. https://doi.org/10.1175/BAMS-D-24-0051.1

Mao, X., Xing, L., Shang, W., Li, S., & Duan, K. (2024). Moisture sources for precipitation over the Pamirs Plateau in winter and spring. *Quarterly Journal of the Royal Meteorological Society*, *150*(759), 820–833. https://doi.org/10.1002/qj.4624

NOAA. (2002). The weekly NOAA optimum interpolation sea surface temperature (OISST) [Dataset]. Retrieved from https://psl.noaa.gov/data/gridded/data.noaa.oisst.v2.html

Oleson, K., Lawrence, D., Bonan, G., Drewniak, B., Huang, M., Koven, C., et al. (2013). *Technical description of version 4.5 of the community land model (CLM)*. National Center for Atmospheric Research. NCAR technical note NCAR/TN-503 + STR.

Pal, J., Small, E., & Eltahir, E. (2000). Simulation of regional-scale water and energy budgets: Representation of subgrid cloud and precipitation processes within RegCM. *Journal of Geophysical Research*, *105*(D24), 29579–29594. https://doi.org/10.1029/2000JD900415

Rahimi, S., Wu, C., Liu, X., & Brown, H. (2019). Exploring a variable-resolution approach for simulating regional climate over the Tibetan Plateau using VR-CESM. *Journal of Geophysical Research: Atmospheres*, *124*(8), 4490–4513. https://doi.org/10.1029/2018JD028925

Reynolds, R. W., Rayner, N. A., Smith, T. M., Stokes, D. C., & Wang, W. (2002). An improved in situ and satellite SST analysis for climate. *Journal of Climate*, *15*(13), 1609–1625. https://doi.org/10.1175/1520-0442(2002)015<1609:aiisas>2.0.co;2;2

Sandu, I., Bechtold, P., Beljaars, A., Bozzo, A., Pithan, F., Shepherd, T., & Zadra, A. (2016). Impacts of parameterized orographic drag on the Northern Hemisphere winter circulation. *Journal of Advances in Modeling Earth Systems*, *8*(1), 196–211. https://doi.org/10.1002/2015MS000564

Seager, R., Naik, N., & Vecchi, G. A. (2010). Thermodynamic and dynamic mechanisms for large-scale changes in the hydrological cycle in response to global warming. *Journal of Climate*, *23*(17), 4651–4668. https://doi.org/10.1175/2010JCLI3655.1

Su, F., Duan, X., Chen, D., Hao, Z., & Cuo, L. (2013). Evaluation of the global climate models in the CMIP5 over the Tibetan Plateau. *Journal of Climate*, *26*(10), 3187–3208. https://doi.org/10.1175/JCLI-D-12-00321.1

Taylor, K. (2001). Summarizing multiple aspects of model performance in a single diagram. *Journal of Geophysical Research*, *106*(D7), 7183–7192. https://doi.org/10.1029/2000JD900719

Tiedtke, M. (1996). An extension of cloud-radiation parameterization in the ECMWF model: The representation of subgrid-scale variations of optical depth. *Monthly Weather Review*, *124*(4), 745–750. https://doi.org/10.1175/1520-0493(1996)124<0745:aeocrp>2.0.co;2

Wang, Q., Yi, S., & Sun, W. (2017). Precipitation-driven glacier changes in the Pamir and Hindu Kush mountains. *Geophysical Research Letters*, *44*(6), 2817–2824. https://doi.org/10.1002/2017GL072646

Wang, X., Chen, D., Pang, G., Anwar, S., Ou, T., & Yang, M. (2021). Effects of cumulus parameterization and land-surface hydrology schemes on Tibetan Plateau climate simulation during the wet season: Insights from the RegCM4 model. *Climate Dynamics*, *57*(7), 1853–1879. https://doi.org/10.1007/s00382-021-05781-1

Wang, Y., Yang, K., Zhou, X., Chen, D., Lu, H., Ouyang, L., et al. (2020). Synergy of orographic drag parameterization and high resolution greatly reduces biases of WRF-simulated precipitation in central Himalaya. *Climate Dynamics*, *54*(3–4), 1729–1740. https://doi.org/10.1007/s00382-019-05080-w

Weissel, J., Pratson, L., & Malinverno, A. (1994). The length-scaling properties of topography. *Journal of Geophysical Research*, *99*(B7), 13997–14012. https://doi.org/10.1029/94jb00130

Wilson, J. (2002). Representing drag on unresolved terrain as a distributed momentum sink. *Journal of the Atmospheric Sciences*, *59*(9), 1629–1637. https://doi.org/10.1175/1520-0469(2002)059<1629:Rdouta>2.0.Co;2

Wood, N., Brown, A., & Hewer, F. (2001). Parametrizing the effects of orography on the boundary layer: An alternative to effective roughness lengths. *Quarterly Journal of the Royal Meteorological Society*, *127*(573), 759–777. https://doi.org/10.1256/smsqj.57302

Wu, F., Fang, X., Yang, Y., Dupont-Nivet, G., Nie, J., Fluteau, F., et al. (2022). Reorganization of Asian climate in relation to Tibetan Plateau uplift. *Nature Reviews Earth & Environment*, *3*(10), 684–700. https://doi.org/10.1038/s43017-022-00331-7

Xu, X., Huang, A., Zhao, W., Yang, B., Xue, D., & Zhang, Y. (2024). Roles of the Tibetan Plateau and Yunnan-Guizhou Plateau in the regional extreme precipitation over Sichuan Basin in summer: A case study. *Journal of Geophysical Research: Atmospheres*, *129*(3), e2023JD039776. https://doi.org/10.1029/2023JD039776

Xue, H., & Shen, X. (2023). A turbulent orographic form drag scheme accounting for anisotropy and orientation for kilometer-to subkilometer-scale models. *Quarterly Journal of the Royal Meteorological Society*, *149*(755), 2527–2549. https://doi.org/10.1002/qj.4519

Xue, H., Zhou, X., Luo, Y., & Yin, J. (2021). Impact of parameterizing the turbulent orographic form drag on convection-permitting simulations of winds and precipitation over South China during the 2019 pre-summer rainy season. *Atmospheric Research*, *263*, 105814. https://doi.org/10.1016/j.atmosres.2021.105814

Yang, K., & Wang, C. (2022). East–West reverse coupling between spring soil moisture and summer precipitation and its possible responsibility for wet bias in GCMs over Tibetan Plateau. *Journal of Geophysical Research: Atmospheres*, *127*(7), e2021JD036286. https://doi.org/10.1029/2021JD036286

Young, G., & Pielke, R. (1983). Application of terrain height variance spectra to mesoscale modeling. *Journal of the Atmospheric Sciences*, *40*(10), 2555–2560. https://doi.org/10.1175/1520-0469(1983)040<2555:Aothvs>2.0.Co;2

Yue, S., Yang, K., Lu, H., Zhou, X., Chen, D., & Guo, W. (2021). Representation of stony surface-atmosphere interactions in WRF reduces cold and wet biases for the Southern Tibetan Plateau. *Journal of Geophysical Research: Atmospheres*, *126*(21), e2021JD035291. https://doi.org/10.1029/2021JD035291

Zeng, X., Zhao, M., & Dickinson, R. (1998). Intercomparison of bulk aerodynamic algorithms for the computation of sea surface fluxes using TOGA COARE and TAO data. *Journal of Climate*, *11*(10), 2628–2644. https://doi.org/10.1175/1520-0442(1998)011<2628:iobaaf>2.0.co;2;2

Zhao, D., Lin, Y., Dong, W., Qin, Y., Chu, W., Yang, K., et al. (2023). Alleviated WRF summer wet bias over the Tibetan Plateau using a new cloud macrophysics scheme. *Journal of Advances in Modeling Earth Systems*, *15*(10), e2023MS003616. https://doi.org/10.1029/2023MS003616

Zhou, X., Beljaars, A., Wang, Y., Huang, B., Lin, C., Chen, Y., & Wu, H. (2017). Evaluation of WRF simulations with different selections of subgrid orographic drag over the Tibetan Plateau. *Journal of Geophysical Research-Atmospheres*, *122*(18), 9759–9772. https://doi.org/10.1002/2017jd027212

Zhou, X., Yang, K., Beljaars, A., Li, H., Lin, C., Huang, B., & Wang, Y. (2019). Dynamical impact of parameterized turbulent orographic form drag on the simulation of winter precipitation over the western Tibetan Plateau. *Climate Dynamics*, *53*(1), 707–720. https://doi.org/10.1007/s00382-019-04628-0

Zhou, X., Yang, K., & Wang, Y. (2018). Implementation of a turbulent orographic form drag scheme in WRF and its application to the Tibetan Plateau. *Climate Dynamics*, *50*(7–8), 2443–2455. https://doi.org/10.1007/s00382-017-3677-y

Zhou, Y., Huang, A., Li, X., Gu, C., & Wu, Y. (2024). Local and remote effects of the sub-grid turbulent orographic form drag on the summer monsoon precipitation over Eastern China. *Journal of Geophysical Research: Atmospheres*, *129*(20), e2024JD041173. https://doi.org/10.1029/2024JD041173

Zou, L., & Zhou, T. (2024). Convection-permitting simulations of current and future climates over the Tibetan Plateau. *Advances in Atmospheric Sciences*, *41*(10), 1901–1916. https://doi.org/10.1007/s00376-024-3277-9